


Article

# Structural and Magnetic Property of Cr<sup>3+</sup> Substituted Cobalt Ferrite Nanomaterials Prepared by the Sol-Gel Method

Jinpei Lin <sup>1,2,†</sup>, Jiaqi Zhang <sup>1,2,†</sup>, Hao Sun <sup>1</sup>, Qing Lin <sup>1,2,\*</sup> , Zeping Guo <sup>3</sup>, Hu Yang <sup>3</sup> and Yun He <sup>1,4,\*</sup>

<sup>1</sup> Guangxi Key Laboratory of Nuclear Physics and Nuclear Technology, Guangxi Normal University, Guilin 541004, China; linjinpei.2007@163.com (J.L.); linqinglab@126.com (J.Z.); heyunlab@163.com (H.S.)

<sup>2</sup> College of Medical Informatics, Hainan Medical University, Haikou 571199, China

<sup>3</sup> College of Physics and Technology, Guangxi Normal University, Guilin 541004, China; zepingguo@mailbox.gxnu.edu.cn (Z.G.); yanghu000@126.com (H.Y.)

<sup>4</sup> State Key Laboratory for Chemistry and Molecular Engineering of Medicinal Resources, Guangxi Normal University, Guilin 541004, China

\* Correspondence: elinqing@126.com (Q.L.); hy@gxnu.edu.cn (Y.H.)

† These authors contributed equally to this work.

Received: 18 August 2018; Accepted: 23 October 2018; Published: 25 October 2018



**Abstract:** Cobalt-chromium ferrite, CoCr<sub>x</sub>Fe<sub>2-x</sub>O<sub>4</sub> ( $x = 0-1.2$ ), has been synthesized by the sol-gel auto-combustion method. X-ray diffraction (XRD) indicates that samples calcined at 800 °C for 3 h were a single-cubic phase. The lattice parameter decreased with increasing Cr concentration. Scanning electron microscopy (SEM) confirmed that the sample powders were nanoparticles. It was confirmed from the room temperature Mössbauer spectra that transition from the ferrimagnetic state to the superparamagnetic state occurred with the doping of chromium. Both the saturation magnetization and the coercivity decreased with the chromium doping. With a higher annealing temperature, the saturation magnetization increased and the coercivity increased initially and then decreased for CoCr<sub>0.2</sub>Fe<sub>1.8</sub>O<sub>4</sub>.

**Keywords:** Co-Cr-Ferrite; sol-gel auto-combustion; nanoparticle structure; Mössbauer; superparamagnetic

## 1. Introduction

Ferrite is an important magnetic material. Cobalt ferrite is a hard magnetic ferrite. It has a high coercivity of 5000 Oe, a moderate saturation magnetization of about 80 emu/g, a high Curie temperature ( $T_C$ ) of 520 °C, and a high anisotropy constant of  $2.65 \times 10^6$  to  $5.1 \times 10^6$  erg/cm<sup>3</sup> [1,2]. Moreover, cobalt ferrite exhibits good insulation, and excellent chemical stability and physical hardness [1–3]. Hard magnetic cobalt ferrite has been widely used as a high-density magnetic recording medium in magnetic recording [4].

It is well known that the chromium ions can control the magnetic parameters of developing technological materials. Cr<sup>3+</sup> ions that are substituted for Fe<sup>3+</sup> ions will change magnetic properties markedly due to their nonmagnetic nature [5,6]. Kwang et al. [6] studied the magnetic properties of ferrite powders, such as CoCr<sub>x</sub>Fe<sub>2-x</sub>O<sub>4</sub>, with increasing Cr content, and the Mössbauer spectra varied from Zeeman sextets to a relaxed doublet for CoCr<sub>x</sub>Fe<sub>2-x</sub>O<sub>4</sub>. The Mössbauer spectra of non-magnetic Zn<sup>2+</sup> ions substituted for Co-ferrite also transitioned from sextets to doublets [7,8]. Muhammad et al. [9] prepared CoCr<sub>x</sub>Fe<sub>2-x</sub>O<sub>4</sub> nanomaterials using the micro-emulsion method, and the Direct current (DC)-electrical resistivity decreased as the temperature increased, indicating the semiconductive nature of the ferrites. Yüksel et al. [10] synthesized nanocrystalline chromium

substituted cobalt ferrite powders by a hydrothermal route. Man et al. [11] investigated the magnetic properties and quantum couplings of spinel ferrite  $\text{CoCr}_x\text{Fe}_{2-x}\text{O}_4$  nanoparticles. However, ferrite powders synthesized via the sol-gel auto-combustion method have good sinterability due to their homogeneous composition and have other advantages of using simple equipment and low material cost [5]. By choosing an appropriate complexing agent and chemical additives, as well as a suitable atmosphere and heating source, it has been possible to affect crystallinity, phase purity, particle size, and defect concentration, thereby influencing the magnetic properties of the ferrite [12].

In the present study, ferrite,  $\text{CoCr}_x\text{Fe}_{2-x}\text{O}_4$  ( $x = 0-1.2$ ), powders were prepared using the sol-gel auto-combustion process. We have investigated the influence of doping content and calcining temperature on the structure by X-ray diffraction and scanning electron microscopy, and studied the magnetic properties of the different calcining temperatures and doping content samples by Mössbauer spectroscopy and a Quantum Design MPMS-XL7 magnetometer. The research purpose is to provide a solid base of knowledge for the synthesis of cobalt ferrite powders that have excellent magnetic properties.

## 2. Methodology

### 2.1. Preparation of Samples

Chromium substituted cobalt ferrite,  $\text{CoCr}_x\text{Fe}_{2-x}\text{O}_4$  ( $x = 0-1.2$ ), powders were prepared by a sol-gel auto-combustion method. Analytical grade chemicals, including cobalt nitrate,  $\text{Co}(\text{NO}_3)_2 \cdot 6\text{H}_2\text{O}$ ; chromium nitrate,  $\text{Cr}(\text{NO}_3)_3 \cdot 9\text{H}_2\text{O}$ ; iron nitrate,  $\text{Fe}(\text{NO}_3)_3 \cdot 9\text{H}_2\text{O}$ ; citric acid,  $(\text{C}_6\text{H}_8\text{O}_7 \cdot \text{H}_2\text{O})$ ; and ammonia,  $(\text{NH}_3 \cdot \text{H}_2\text{O})$ , were used as raw materials, and the citric acid was used as a complexing agent for the spinel ferrite synthesis. The molar ratio of metal nitrates to citric acid was 1:1. Nitrate and citric acid were dissolved in deionized water, respectively. The pH of the metal nitrate was adjusted to an appropriate pH of 7 to 9 by the addition of aqueous ammonia. The mixed solution was placed in an 80-degree water bath for heating in a water bath, and citric acid was gradually added dropwise during the water bath, and the mixed solution was continuously stirred until a wet gel was formed. The wet gel was dried in a digital drying oven at 120 °C for 2 h, and the obtained dry gel was ignited in the air with a combustion improver (anhydrous ethanol) to ignite the self-propagating powder to obtain a fluffy powder. After the powder was ground, the final sample was obtained by calcination at two specific temperatures (400 °C and 800 °C) for 3 h in a muffle furnace.

### 2.2. Characterization

The crystal structure of the sample was analyzed by an X-ray diffractometer (D/max-2500 V/PC, Rigaku, Japan) using a Cu K $\alpha$  target ( $\lambda = 0.15405$  nm). The morphology of the sample was observed by a scanning electron microscope (NoVaTM Nano SEM 430, Thermo Fisher Scientific, Waltham, MA, USA). The Mössbauer spectrum at room temperature was measured using an isothermal accelerated Mössbauer spectrometer (Fast Com Tec PC-mossII, Oberhaching, Germany) with a source of  $^{57}\text{Co}$  and labeled with  $\alpha\text{-Fe}$ . Measurement of hysteresis loops of samples at room temperature was completed using a superconducting quantum interference magnetometer (MPMS-XL-7, Quantum Design, San Diego, CA, USA).

## 3. Results and Discussion

### 3.1. X-ray Diffraction Analysis

Figure 1 shows the XRD diffraction pattern of  $\text{CoCr}_x\text{Fe}_{2-x}\text{O}_4$  ( $x = 0-1.2$ ) ferrite after calcination at 800 °C for 3 h. The results show that all of the ferrites had a single-phase structure. Other impurity peaks were not detected for these samples. Thus, it can be seen that  $\text{Cr}^{3+}$  ion substituted the  $\text{Fe}^{3+}$  ion at the octahedral (B) site and was not influenced by the spinel cubic structure of the cobalt ferrite. When  $0 < x < 1$ , the trend of the lattice parameters was to decrease with increasing chromium

concentration, as shown in Table 1. The decrease in the lattice parameter can be attributed to the substitution of the larger  $\text{Fe}^{3+}$  ions (0.645 Å) by smaller  $\text{Cr}^{3+}$  ions (0.63 Å) [9]. When  $1 < x$ , the increase of lattice parameter is attributed to the elastic strain and magneto-volume effects [12].

The density of X rays is determined by the following formula [13–15]:

$$\rho_x = \frac{8M}{Na^3} \quad (1)$$

where  $a$  is the lattice parameter,  $M$  is relative molecular mass, and  $N$  is the Avogadro number.

The X-ray density decreased with  $\text{Cr}^{3+}$  concentration for all samples, as is evident from Table 1. The atomic weight of Fe is greater than that of Cr, so the relative molecular mass decreases with an increasing content of  $\text{Cr}^{3+}$  ions. The decrease in X-ray density was attributed to the fact that the relative molecular mass decreased more than the negligible decline of the lattice constant.

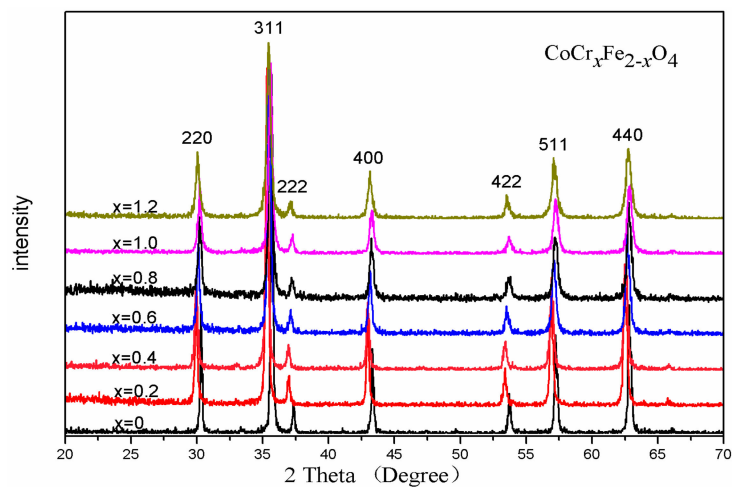


Figure 1. XRD patterns of  $\text{CoCr}_x\text{Fe}_{2-x}\text{O}_4$  calcined at 800 °C.

The average crystallite size consistently decreased with increasing Cr content, as is evident from Table 1, and similar results have been reported in the literature [6]. Figure 2 shows the X-ray diffraction pattern of the sample  $\text{CoCr}_{0.2}\text{Fe}_{1.8}\text{O}_4$  when calcined at different temperatures. All samples were single-phase spinel structures with no heterophases found. The lattice constants of all samples did not show much change. The average crystallite size of  $\text{CoCr}_{0.2}\text{Fe}_{1.8}\text{O}_4$  increased with increasing calcining temperature as can be observed from Table 2.

Table 1. XRD data for  $\text{CoCr}_x\text{Fe}_{2-x}\text{O}_4$  calcined at 800 °C.

Content ( $x$ )	Lattice Parameter (Å)	Average Crystallite Size(Å)	Density ( $\text{g}/\text{cm}^3$ )
0	8.35497	556	5.3468
0.2	8.40877	436	5.2250
0.4	8.40790	382	5.2094
0.6	8.38461	340	5.2355
0.8	8.36538	284	5.2543
1.0	8.36368	276	5.2400
1.2	8.37912	244	5.1937

In other published work [14], the diffraction peaks of  $\text{Ni}_{0.50}\text{Cu}_{0.25}\text{Zn}_{0.25}\text{Cr}_x\text{Fe}_{2-x}\text{O}_4$  calcined at lower temperatures were not very sharp, but in the present study, the diffraction peaks of unsintered  $\text{CoCr}_{0.2}\text{Fe}_{1.8}\text{O}_4$  were very sharp indeed. The chromium-replaced cobalt ferrite powders were prepared using the sol-gel auto-combustion process, and before calcining, the samples had excellent crystallinity.

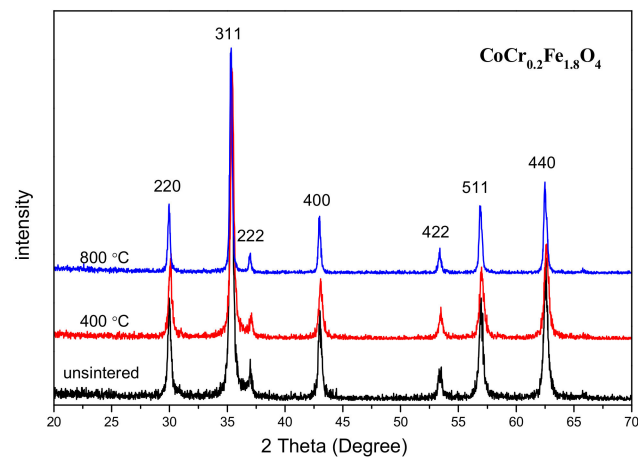


Figure 2. XRD patterns of  $\text{CoCr}_{0.2}\text{Fe}_{1.8}\text{O}_4$  calcined at different temperatures.

Table 2. XRD data for  $\text{CoCr}_{0.2}\text{Fe}_{1.8}\text{O}_4$  calcined at different temperatures.

Temperature (°C)	Lattice Parameter (Å)	Average Crystallite Size (Å)	Density ( $\text{g}/\text{cm}^3$ )
unsintered	8.40551	280	5.2311
400	8.39683	313	5.2473
800	8.40877	436	5.2250

### 3.2. Scanning Electron Microscopy (SEM)

The SEM micrographs of  $\text{CoCr}_x\text{Fe}_{2-x}\text{O}_4$  ( $x = 0, 0.2$ ) ferrites annealed at 800 °C for 3 h are shown in Figure 3. It can be observed that the grain size is almost uniform and the material is well crystallized for  $\text{CoCr}_x\text{Fe}_{2-x}\text{O}_4$  ( $x = 0, 0.2$ ). Histograms of the comparative grain size distributions of  $\text{CoFe}_2\text{O}_4$  ( $x = 0$ ) and  $\text{CoCr}_x\text{Fe}_{2-x}\text{O}_4$  ( $x = 0, 0.2$ ) ferrites are shown in Figure 4. The average particle sizes of  $\text{CoFe}_2\text{O}_4$  and  $\text{CoCr}_x\text{Fe}_{2-x}\text{O}_4$  were estimated by a statistical average method to be approximately 96.26 and 51.76 nm, respectively. This shows that the prepared ferrite powders were nanoparticles and that the average grain size decreased significantly by increasing the Cr content, which can be due to the ionic radius of iron atoms being larger than the ionic radius of chromium atoms. The average crystallite size was determined by XRD to be slightly smaller than the average grain size [15].

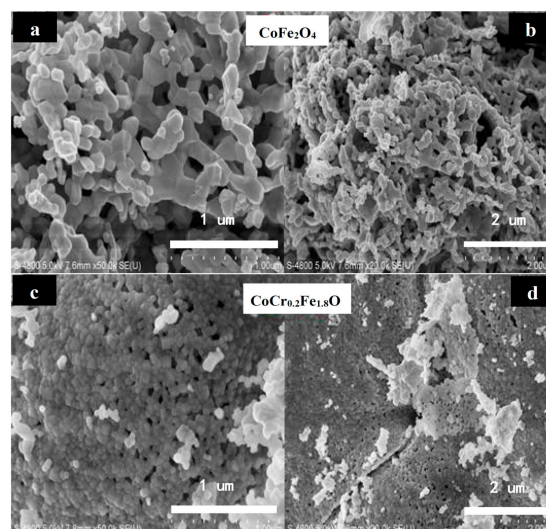
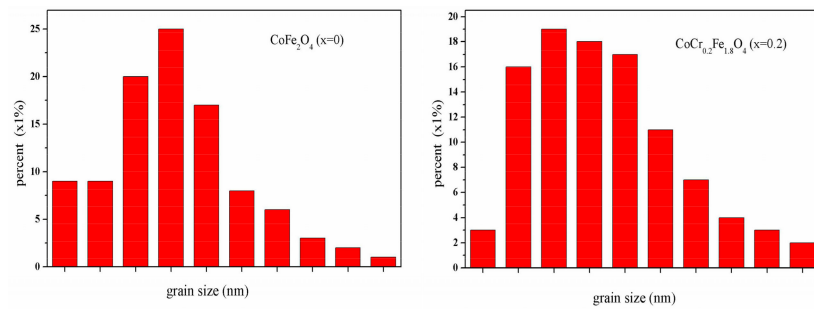


Figure 3. SEM micrographs depict of  $\text{CoFe}_2\text{O}_4$  ( $x = 0$ ) and  $\text{CoCr}_{0.2}\text{Fe}_{1.8}\text{O}_4$  ( $x = 0.2$ ) ferrites with diameters of 1  $\mu\text{m}$  (a), 2  $\mu\text{m}$  (b), 1  $\mu\text{m}$  (c), and 2  $\mu\text{m}$  (d).



**Figure 4.** The grain size distributions of  $\text{CoFe}_2\text{O}_4$  and  $\text{CoCr}_{0.2}\text{Fe}_{1.8}\text{O}_4$  after calcination at  $800^\circ\text{C}$ .

### 3.3. Mössbauer Spectroscopy

The room temperature Mössbauer spectra for  $\text{CoCr}_x\text{Fe}_{2-x}\text{O}_4$  are shown in Figure 5. The data of all samples were analyzed using Mösswinn 3.0 software. When  $0 \leq x \leq 0.6$ , the spectrum of the sample  $\text{CoCr}_x\text{Fe}_{2-x}\text{O}_4$  is fitted with two sets of six-line peaks, because  $\text{Fe}^{3+}$  takes the tetrahedral A at the B-position of the octahedron. This indicates the ferromagnetic properties of the sample. Among them, the six-line peak of the B position is larger in the isomer shift (I.S.), and the six-line peak of the A position is smaller. This is because the bond length of the tetrahedral A site  $\text{Fe}^{3+}\text{-O}^{2-}$  is smaller than the bond length of the octahedral B site  $\text{Fe}^{3+}\text{-O}^{2-}$ , and the orbital overlap of the A site  $\text{Fe}^{3+}\text{-O}^{2-}$  is larger; that is, the A site is more covalent than the B site. The covalency is large, so the isomer shift (I.S.) of the B position is larger [6]. Other studies have shown that the isomer shift (I.S.) value of  $\text{Fe}^{3+}$  ions is 0.1 to 0.5 mm/s, while for  $\text{Fe}^{2+}$ , it is 0.6 to 1.7 mm/s [16]. From Table 3, values for I.S. in the present study indicate that iron is in the  $\text{Fe}^{3+}$  state.

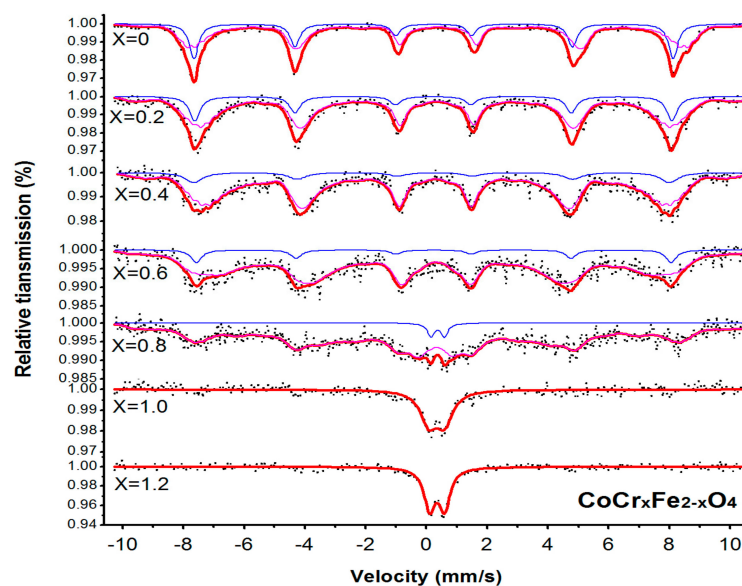


**Figure 5.** Room temperature Mössbauer spectra for  $\text{CoCr}_x\text{Fe}_{2-x}\text{O}_4$  calcined at  $800^\circ\text{C}$ .

The values of the magnetic hyperfine field at the A and B sites decrease with increasing chromium substitution, and for the hyperfine field of the octahedral B site, the decrease is more evident, as shown in Table 3. The observed decrease in the octahedral magnetic hyperfine field with the increasing of  $\text{Cr}^{3+}$  ions is due to the decrease in the A-B exchange interactions, which results in the lower magnetic hyperfine field [6,17]. In all the samples, the quadrupole shift of the A and B magnetic sextet was very small, which indicated that the ferrites were in close cubic symmetry [18,19].

For the  $\text{CoCr}_x\text{Fe}_{2-x}\text{O}_4$  with  $x = 0.8$ , the Mössbauer spectrum exhibits the characteristics of the Magnetic effect, which consists of a set of six-line peaks and a set of paramagnetic doublets. The samples transformed into a mixed state of superparamagnetic and magnetic orders from the

initial magnetic order. Mössbauer spectra of the samples with  $x = 1.0, 1.2$  consisted only of a central doublet, and it exhibited super-paramagnetic characteristics. This was attributed to the reduction of the magnetic interactions between iron ions with greater  $\text{Cr}^{3+}$  dilution. The decrease in the line width of this doublet exhibited increased relative intensity due to the increase in the substituted Cr content [17].

**Table 3.** Mössbauer parameters of isomer shift (IS), quadrupole splitting (QS), magnetic hyperfine field (H), linewidth ( $\Gamma$ ), and absorption area ( $A_0$ ) for  $\text{CoCr}_x\text{Fe}_{2-x}\text{O}_4$  annealed at 800 °C.

Content (x)	Component	I.S. (mm/s)	Q.S. (mm/s)	H (T)	$\Gamma$ (mm/s)	$A_0$ (mm/s)
0	Sextet (A)	0.237	−0.004	48.946	0.360	32.4
	Sextet (B)	0.375	−0.024	45.695	0.322	67.6
0.2	Sextet (A)	0.223	0.007	48.724	0.409	20.1
	Sextet (B)	0.317	−0.065	44.454	0.355	79.9
0.4	Sextet (A)	0.222	−0.112	48.581	0.662	11.8
	Sextet (B)	0.303	0.011	43.279	0.347	88.2
0.6	Sextet (A)	0.235	0.010	48.473	0.408	7.6
	Sextet (B)	0.303	−0.059	39.210	0.437	92.4
0.8	Sextet (B)	0.327	0.074	34.844	0.418	97.0
	Double	0.373	0.437	-	0.271	3.0
1.0	Double	0.336	0.520	-	0.663	100
1.2	Double	0.351	0.491	-	0.444	100

The room temperature Mössbauer spectrum of  $\text{CoCr}_{0.2}\text{Fe}_{1.8}\text{O}_4$  calcined at different temperatures are displayed in Figure 6. All the Mössbauer spectra were fitted with two sextet sub-patterns. Table 4 shows the magnetic hyperfine field increased slightly with the annealing temperature. The results of XRD analysis showed that the samples were well crystallized at different temperatures, and the average grain size became larger as the calcination temperature increased. The magnetic hyperfine field of the sample increases as the calcination temperature increases. Therefore, the change of the magnetic hyperfine field can be explained as the average grain size caused by the change of the calcination temperature [8]. The absorption area of Mössbauer energy for  $\text{CoCr}_{0.2}\text{Fe}_{1.8}\text{O}_4$  calcined at different temperatures exhibited certain changes, which indicated that the calcining temperature influenced the fraction of the  $\text{Fe}^{3+}$  ions in the tetrahedral A and octahedral B sites [6,20,21].

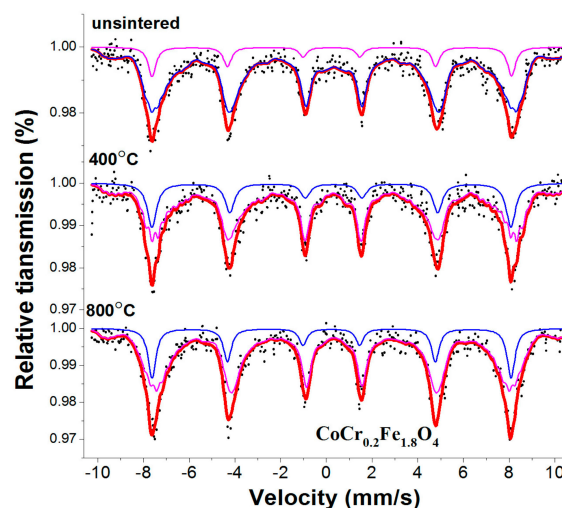


**Figure 6.** Room temperature Mössbauer spectra for  $\text{CoCr}_{0.2}\text{Fe}_{1.8}\text{O}_4$  calcined at different temperatures.

**Table 4.** Mössbauer parameters of isomer shift (IS), quadrupole splitting (QS), magnetic hyperfine field (H), linewidth ( $\Gamma$ ), and absorption area ( $A_0$ ) for  $\text{CoCr}_x\text{Fe}_{2-x}\text{O}_4$  annealed at different temperature.

Temperature ( $^{\circ}\text{C}$ )	Component	I.S. (mm/s)	Q.S. (mm/s)	H (T)	$\Gamma$ (mm/s)	$A_0$ (mm/s)
unsintered	Sextet (A)	0.234	0.009	48.790	0.412	11.8
	Sextet (B)	0.336	-0.004	43.424	0.386	88.2
400	Sextet (A)	0.273	-0.104	48.716	0.491	21.8
	Sextet (B)	0.325	0.051	43.557	0.283	78.2
800	Sextet (A)	0.223	0.007	48.724	0.409	20.1
	Sextet (B)	0.317	-0.065	44.454	0.355	79.9

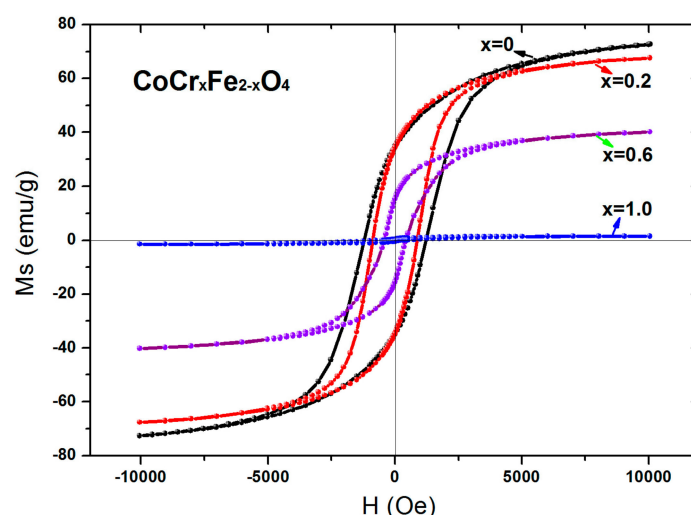
### 3.4. Magnetic Analysis

The magnetic hysteresis loops for  $\text{CoCr}_x\text{Fe}_{2-x}\text{O}_4$  at room temperature are shown in Figure 7. For all samples, magnetization reached saturation at a magnetic field of 10,000 Oe. It can be observed from Table 5 that the saturation magnetization of the sample decreases with the substitution of chromium ions. The saturation magnetization of the sample is expressed as the following relationship [5]:

$$\sigma_s = \frac{5585 \times n_B}{M} \quad (2)$$

where  $n_B$  is the magnetic moment in terms of Bohr magnetons, and  $M$  is the relative molecular mass. With the substitution of chromium ions, the relative molecular mass of the sample  $\text{CoCr}_x\text{Fe}_{2-x}\text{O}_4$  decreases, and the change in magnetic moment can be explained by the Néel theory. The ionic magnetic moments of the  $\text{Cr}^{3+}$ ,  $\text{Co}^{2+}$ , and  $\text{Fe}^{3+}$  ions are  $3\mu_B$ ,  $3\mu_B$ , and  $5\mu_B$  [5,9,13], respectively. According to the two-sublattice model of Néel's theory [14,19], using the cation distribution of  $(\text{Fe})_A[\text{CoCr}_x\text{Fe}_{1-x}]_B\text{O}_4$ , the  $\text{Co}^{2+}$  ions prefer to occupy the octahedral site (B) in the  $\text{CoFe}_2\text{O}_4$  material with an inverse spinel structure [1,2], and  $\text{Cr}^{3+}$  ions have a tendency to occupy the B-site [5,10,20]. The magnetic moment,  $n_B$ , therefore, can be expressed as [5,10,13]:

$$n_B = M_B - M_A = 3 + 3x + 5(1 - x) - 5 = 3 - 2x \quad (3)$$

**Figure 7.** Room temperature magnetic hysteresis loops for  $\text{CoCr}_x\text{Fe}_{2-x}\text{O}_4$  calcined at 800  $^{\circ}\text{C}$ .

The  $M_B$  and  $M_A$  in the formula are the B-position of the octahedral lattice and the A-site of the tetrahedral lattice [21,22]. Figure 8 shows the variation of the total magnetic moment obtained by theoretical calculations with chromium substitution.

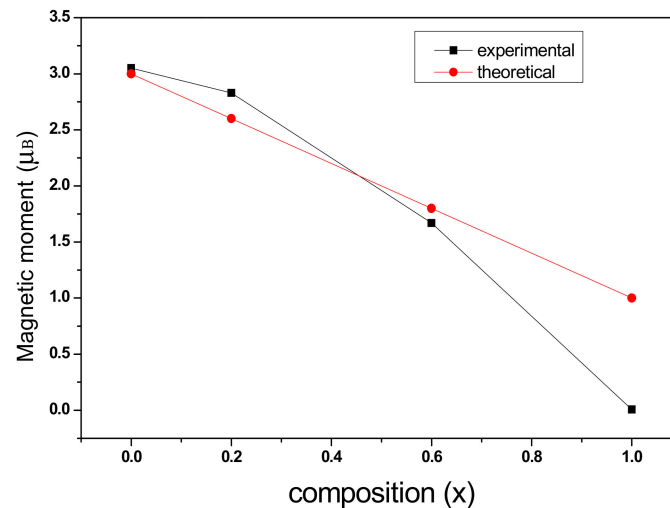


**Figure 8.** Variation in experimental and theoretical magnetic moments with chromium content ( $x$ ).

As can be seen from Figure 8, the experimental magnetic moment and the theoretical magnetic moment decreases as the Cr content,  $x$ , increases, and according to the relationship (2), the theoretical saturation magnetization decreases with increasing chromium concentration. The saturation magnetization obtained by the experiment is in accordance with the theoretical analysis for all samples.

**Table 5.** Magnetic data for  $\text{CoCr}_x\text{Fe}_{2-x}\text{O}_4$  calcined at 800 °C.

Content ( $x$ )	$M_s$ (emu/g)	$H_c$ (Oe)	$M_r$ (emu/g)	$n_B$
0	72.58	1005.33	34.71	3.05
0.2	67.66	878.10	34.39	2.83
0.6	40.20	401.44	15.51	1.67
1.0	1.51	301.20	0.39	0.006

It can be observed from Table 5 that the coercive force of the sample  $\text{CoCr}_x\text{Fe}_{2-x}\text{O}_4$  decreases with the doping of chromium. The large coercivity originates from the anisotropy of the  $\text{Co}^{3+}$  ions in the octahedral (B) site as a result of their octahedral lattice having strong spin-orbit coupling [9,23]. The decreasing of coercivity associated with the doping of chromium in the  $\text{CoCr}_x\text{Fe}_{2-x}\text{O}_4$  ferrite may be attributed to  $\text{Co}^{2+}$  ion migration to the tetrahedral site, leading to the observed loss in anisotropy. The magnetocrystalline anisotropy of the Cr ferrites was negative [24,25]. Therefore, the magnetic anisotropy decreased with increasing Cr content, which leads to the decrease in coercivity [26,27].

The room temperature magnetic hysteresis loops for un-sintered  $\text{CoCr}_{0.2}\text{Fe}_{1.8}\text{O}_4$  and for the same material after annealing at 400 °C and 800 °C are displayed in Figure 9. The data summarized in Table 6 indicate that saturation magnetization of the  $\text{CoCr}_{0.2}\text{Fe}_{1.8}\text{O}_4$  increased with annealing temperature, which was attributed to the increase in particle size [13]. During the annealing process, the net reduction of the free energy of the solid-solid interface and the free energy of the solid-vapor interface is the driving force for grain growth [13,28]. The coercivity of the  $\text{CoCr}_{0.2}\text{Fe}_{1.8}\text{O}_4$  initially increased and then decreased as the annealing temperature was increased. This can be explained by the associated variation in grain size [29,30]. In the range of single domain sizes, the coercive force can be expressed as  $H_C = g - h/D^2$ . In the range of multi-domain sizes, the coercive force can be written as  $H_C = a + b/D$  as the particle size changes. “ $g, h, a, b$ ” in the formula are constants, and “ $D$ ” is the diameter of the particles [21,31]. Therefore, as the particle size becomes larger in the single domain range, the coercive force becomes larger; and in the multidomain range, as the particle size increases, the coercive force decreases [32,33]. In the present study, the grain size of  $\text{CoCr}_{0.2}\text{Fe}_{1.8}\text{O}_4$  calcined at



different temperatures may lie in the single domain region or the multi-domain region, so coercivity increases initially and then decreases as the annealing temperature is increased [34].

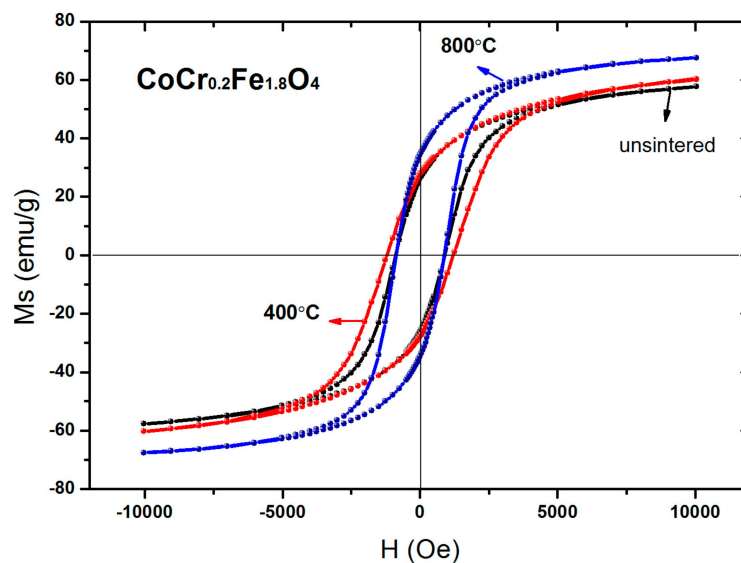


**Figure 9.** Room temperature hysteresis loops of  $\text{CoCr}_{0.2}\text{Fe}_{1.8}\text{O}_4$  calcined at different temperatures.

**Table 6.** Magnetic data for  $\text{CoCr}_{0.2}\text{Fe}_{1.8}\text{O}_4$  calcined at different temperatures.

Temperature ( $^{\circ}\text{C}$ )	$M_s$ (emu/g)	$H_c$ (Oe)	$M_r$ (emu/g)	$n_B$
unsintered	57.74	877.06	26.20	2.42
400	60.35	1254.18	27.75	2.53
800	67.66	878.10	34.39	2.83

#### 4. Conclusions

The analysis results of the XRD diffraction pattern show that the  $\text{CoCr}_x\text{Fe}_{2-x}\text{O}_4$  calcined at  $800^{\circ}\text{C}$  was a single phase spinel structure. The lattice constant of  $\text{CoCr}_x\text{Fe}_{2-x}\text{O}_4$  becomes smaller with the substitution of chromium ions because the radius of chromium ions is smaller than the radius of iron ions. The XRD diffraction pattern of  $\text{CoCr}_{0.2}\text{Fe}_{1.8}\text{O}_4$  calcined at different temperatures showed that the sample prepared by the sol-gel self-propagation method had good crystallinity even without calcination. The results of SEM showed that the particles of the prepared sample were distributed in an almost uniform size, and crystallized well. The room temperature Mössbauer analysis of  $\text{CoCr}_x\text{Fe}_{2-x}\text{O}_4$  calcined at  $800^{\circ}\text{C}$  shows that the sample transitions from ferromagnetic to superparamagnetic with the doping of chromium ions. The Mössbauer spectrum of  $\text{CoCr}_{0.2}\text{Fe}_{1.8}\text{O}_4$  calcined at different temperatures indicates that the calcination temperature will have an effect on the magnetic properties. Both saturation magnetization and coercivity decreased with the substitution of chromium ions, and the change in saturation magnetization can be explained by the Néel theory. The coercive force becomes smaller with the substitution of chromium ions due to a decrease in the magnetocrystalline anisotropy constant.

**Author Contributions:** Writing-Original Draft Preparation, Q.L. and Y.H.; Writing-Review & Editing, J.L. and Q.L.; Validation, J.L., J.Z. and H.S.; Methodology, Q.L.; Formal Analysis, Q.L. and J.L.; Resources, Z.G. and Y.H.; J.L. and J.Z. contributed equally to this work. Q.L. and Y.H. are co-corresponding authors contributed equally to this study. All authors discussed the results and commented on the manuscript.

**Funding:** This research was funded by the National Natural Science Foundation of China (No. 11364004, 11775057, 11747307, 11765004, 11547307, 11647309). And the project was funded by Guangxi Key Laboratory of Nuclear Physics and Nuclear Technology.

**Conflicts of Interest:** No potential conflict of interest was reported by the authors.

## References

1. Mohamed, R.M.; Rashada, M.M.; Haraz, F.A.; Sigmund, W. Structure and magnetic properties of nanocrystalline cobalt ferrite powders synthesized using organic acid precursor method. *J. Magn. Magn. Mater.* **2010**, *322*, 2058–2064. [[CrossRef](#)]
2. Amiri, S.; Shokrollahi, H. The role of cobalt ferrite magnetic nanoparticles in medical science. *Mater. Sci. Eng. C* **2013**, *33*, 1–8. [[CrossRef](#)] [[PubMed](#)]
3. Sanpo, N.; Berndt, C.C.; Wen, C.; Wang, J. Transition metal-substituted cobalt ferrite nanoparticles for biomedical applications. *Acta Biomater.* **2013**, *9*, 5830–5837. [[CrossRef](#)] [[PubMed](#)]
4. Chia, C.H.; Zakaria, S.; Yusoffa, M.; Goh, S.C.; Haw, C.Y.; Ahmadi, S.; Huang, N.M.; Lim, H.N. Size and crystallinity-dependent magnetic properties of  $\text{CoFe}_2\text{O}_4$  nanocrystals. *Ceram. Int.* **2010**, *36*, 605–609. [[CrossRef](#)]
5. Toksha, B.G.; Shirsath, S.E.; Mane, M.L.; Patange, S.M.; Jadhav, S.S.; Jadhav, K.M. Autocombustion High-Temperature Synthesis, Structural, and Magnetic Properties of  $\text{CoCr}_x\text{Fe}_{2-x}\text{O}_4$  ( $0 \leq x \leq 1.0$ ). *J. Phys. Chem. C* **2011**, *115*, 20905–20912. [[CrossRef](#)]
6. Chae, K.P.; Lee, Y.B.; Lee, J.G.; Lee, S.H. Crystallographic and magnetic properties of  $\text{CoCr}_x\text{Fe}_{2-x}\text{O}_4$  ferrite powders. *J. Magn. Magn. Mater.* **2000**, *220*, 59–64. [[CrossRef](#)]
7. Bayoumi, W. Structural and electrical properties of zinc-substituted cobalt ferrite. *J. Mater. Sci.* **2007**, *42*, 8254–8261. [[CrossRef](#)]
8. Lee, S.W.; Ryu, Y.G.; Yang, K.J. Magnetic properties of  $\text{Zn}^{2+}$  substituted ultrafine Co-ferrite grown by a sol-gel method. *J. Appl. Phys.* **2002**, *91*, 7610–7612. [[CrossRef](#)]
9. Iqbal, M.I.; Siddiquah, M.R. Electrical and magnetic properties of chromium-substituted cobalt ferrite nanomaterials. *J. Alloys Compd.* **2008**, *453*, 513–518. [[CrossRef](#)]
10. Köseoğlu, Y.; Oleiwi, M.I.O.; Yilgin, R.; Kocbay, A.N. Effect of chromium addition on the structural, morphological and magnetic properties of nano-crystalline cobalt ferrite system. *Ceram. Int.* **2012**, *38*, 6671–6676. [[CrossRef](#)]
11. Han, M.; Vestal, C.R.; Zhang, Z.J. Quantum Couplings and Magnetic Properties of  $\text{CoCr}_x\text{Fe}_{2-x}\text{O}_4$  ( $0 < x < 1$ ) Spinel Ferrite Nanoparticles Synthesized with Reverse Micelle Method. *J. Phys. Chem. B* **2004**, *108*, 583–587.
12. Rizal, C.; Kolthammer, J.; Pokharel, R.K.; Choi, B.C. Magnetic properties of nanostructured Fe-Co alloys. *J. Appl. Phys.* **2013**, *113*, 113905. [[CrossRef](#)]
13. Singhal, S.; Jauhar, S.; Singh, J.; Chandra, K.; Bansal, S. Investigation of structural, magnetic, electrical and optical properties of chromium substituted cobalt ferrites ( $\text{CoCr}_x\text{Fe}_{2-x}\text{O}_4$ ,  $0 \leq x \leq 1$ ) synthesized using sol gel auto combustion method. *J. Mol. Struct.* **2012**, *1012*, 182–188. [[CrossRef](#)]
14. Bayoumy, W.A.; Gabal, M.A. Synthesis characterization and magnetic properties of Cr-substituted NiCuZn nanocrystalline ferrite. *J. Alloys Compd.* **2010**, *506*, 205–209. [[CrossRef](#)]
15. Lin, Q.; Xu, J.; Yang, F.; Lin, J.; Yang, H.; He, Y. Magnetic and Mössbauer Spectroscopy Studies of Zinc-Substituted Cobalt Ferrites Prepared by the Sol-Gel Method. *Materials* **2018**, *11*, 1799. [[CrossRef](#)] [[PubMed](#)]
16. He, Y.; Lei, C.; Lin, Q.; Dong, J.; Yu, Y.; Wang, L. Mössbauer and Structural properties of La-substituted  $\text{Ni}_{0.4}\text{Cu}_{0.2}\text{Zn}_{0.4}\text{Fe}_2\text{O}_4$  nanocrystalline ferrite. *Sci. Adv. Mater.* **2015**, *7*, 1809–1815. [[CrossRef](#)]
17. Gabal, M.A.; Al Angari, Y.M. Low-temperature synthesis of nanocrystalline NiCuZn ferrite and the effect of Cr substitution on its electrical properties. *J. Magn. Magn. Mater.* **2010**, *322*, 3159–3165. [[CrossRef](#)]
18. Lv, H.; Zhang, H.; Zhang, B.; Ji, G.; He, Y.; Lin, Q. A proposed electron transmission mechanism between  $\text{Fe}^{3+}/\text{Co}^{2+}$  and  $\text{Fe}^{3+}/\text{Fe}^{3+}$  in the spinel structure and its practical evidence in quaternary  $\text{Fe}_{0.5}\text{Ni}_{0.5}\text{Co}_2\text{S}_4$ . *J. Mater. Chem. C* **2016**, *4*, 5476–5482. [[CrossRef](#)]
19. Gözüak, F.; köseoğlu, Y.; Baykal, A.; Kavas, H. Synthesis and characterization of  $\text{Co}_{1-x}\text{Zn}_x\text{Fe}_2\text{O}_4$  magnetic nanoparticles via a PEG-assisted route. *J. Magn. Magn. Mater.* **2009**, *321*, 2170–2177. [[CrossRef](#)]
20. Singhal, S.; Barthwal, S.K.; Chandra, K. XRD, magnetic and Mössbauer spectral studies of nano size aluminum substituted cobalt ferrites ( $\text{CoAl}_x\text{Fe}_{2-x}\text{O}_4$ ). *J. Magn. Magn. Mater.* **2006**, *306*, 233–240. [[CrossRef](#)]
21. He, Y.; Yang, X.; Lin, J.; Lin, Q.; Dong, J. Mössbauer spectroscopy, Structural and magnetic studies of  $\text{Zn}^{2+}$  substituted magnesium ferrite nanomaterials prepared by Sol-Gel method. *J. Nanomater.* **2015**, *2015*, 854840. [[CrossRef](#)]

22. Bhukal, S.; Namgyal, T.; Mor, S.; Bansal, S.; Singhal, S. Structural, electrical, optical and magnetic properties of chromium substituted Co-Zn nanoferrites  $\text{Co}_{0.6}\text{Zn}_{0.4}\text{Cr}_x\text{Fe}_{2-x}\text{O}_4$  ( $0 \leq x \leq 1.0$ ) prepared via sol-gel auto-combustion method. *J. Mol. Struct.* **2012**, *1012*, 162–167. [[CrossRef](#)]
23. Gabal, M.A.; Al Angari, Y.M.; Al-Agel, F.A. Synthesis, characterization and magnetic properties of Cr-substituted Co-Zn ferrites Nanopowders. *J. Mol. Struct.* **2013**, *1035*, 341–347. [[CrossRef](#)]
24. Lin, Q.; Lei, C.; He, Y.; Xu, J.; Wang, R. Mössbauer and XRD studies of  $\text{Ni}_{0.6}\text{Cu}_{0.2}\text{Zn}_{0.2}\text{Ce}_x\text{Fe}_{2-x}\text{O}_4$  ferrites by Sol-Gel auto-combustion. *J. Nanosci. Nanotechnol.* **2015**, *15*, 2997–3003. [[CrossRef](#)] [[PubMed](#)]
25. Shabrawy, S.E.I.; Bocker, C.; Tzankov, D.; Georgieva, M.; Harizanova, R.; Rüssel, C. The effect of zinc substitution on the magnetism of magnesium ferrite nanostructures crystallized from borate glasses. *Ceram. Int.* **2017**, *43*, 3804–3810. [[CrossRef](#)]
26. Motavallian, P.; Abasht, B.; Abdollah-Pour, H. Zr doping dependence of structural and magnetic properties of cobalt ferrite synthesized by sol-gel based Pechini method. *J. Magn. Magn. Mater.* **2018**, *451*, 577–586. [[CrossRef](#)]
27. Ahmad, S.; Kumar, D.; Syed, I.; Satar, R.; Ansari, S. Structural, Spectroscopic and Magnetic Study of Nanocrystalline Cerium-Substituted Magnesium Ferrites. *Arab. J. Sci. Eng.* **2016**, *42*, 1–10. [[CrossRef](#)]
28. Sutka, A.; Mezinskis, G. Sol-gel auto-combustion synthesis of spinel-type ferrite nanomaterials. *Front. Mater. Sci.* **2012**, *6*, 128–141. [[CrossRef](#)]
29. Ahmad, N.; Alam, M.; Ansari, A.A.; Alrayes, B.F.; Ahmed, M.; Alotaibi, M.A. Nickel Ferrite Nanomaterials: Synthesis, Characterization and Properties. *Nanosci. Nanotechnol. Lett.* **2017**, *9*, 1688–1695. [[CrossRef](#)]
30. Borhan, A.I.; Slatineanu, T.; Jordan, A.R.; Palamaru, M.N. Influence of chromium ion substitution on the structure and properties of zinc ferrite synthesized by the sol-gel auto-combustion method. *Polyhedron* **2013**, *56*, 82–89. [[CrossRef](#)]
31. Kumar, A.; Shen, J.; Yang, W.; Zhao, H.; Sharma, P.; Varshney, D.; Li, Q. Impact of Rare Earth  $\text{Gd}^{3+}$  Ions on Structural and Magnetic Properties of  $\text{Ni}_{0.5}\text{Zn}_{0.5}\text{Fe}_{2-x}\text{Gd}_x\text{O}_4$  Spinel Ferrite: Useful for Advanced Spintronic Technologies. *J. Supercond. Nov. Magn.* **2018**, *31*, 1173–1182. [[CrossRef](#)]
32. Harzali, H.; Marzouki, A.; Saida, F.; Megriche, A.; Mgaidi, A. Structural, magnetic and optical properties of nanosized  $\text{Ni}_{0.4}\text{Cu}_{0.2}\text{Zn}_{0.4}\text{R}_{0.05}\text{Fe}_{1.95}\text{O}_4$  ( $\text{R} = \text{Eu}^{3+}, \text{Sm}^{3+}, \text{Gd}^{3+}$  and  $\text{Pr}^{3+}$ ) ferrites synthesized by co-precipitation method with ultrasound irradiation. *J. Magn. Magn. Mater.* **2018**, *460*, 89–94. [[CrossRef](#)]
33. Ahmad, S.I.; Ansari, S.A.; Kumar, D.R. Structural, morphological, magnetic properties and cation distribution of Ce and Sm co-substituted nano crystalline cobalt ferrite. *Mater. Chem. Phys.* **2018**, *208*, 248–257. [[CrossRef](#)]
34. Lin, J.; He, Y.; Du, X.; Lin, Q.; Yang, H.; Shen, H. Structural and Magnetic Studies of  $\text{Cr}^{3+}$  Substituted Nickel Ferrite Nanomaterials Prepared by Sol-Gel Auto-Combustion. *Crystals* **2018**, *8*, 384. [[CrossRef](#)]

